

*Full Paper*

## **The Study of a New Pyran Compound in Two Distinct Environments: 0.5 M H<sub>2</sub>SO<sub>4</sub> And 1.0 M HCl As an Inhibitor and Combines Experimental Evaluations with Computational Analytics to Assess Its Performance**

**M. Khattabi,<sup>1</sup> F. Benhiba,<sup>2,3</sup> S. Tabti,<sup>4</sup> A. Djedouani,<sup>5,6</sup> H. Zarrok,<sup>1</sup> A. Boutakiout,<sup>2</sup> R. Touzani,<sup>7</sup> I. Warad,<sup>8</sup> M. Ebn Touhami,<sup>1</sup> H. Oudda,<sup>1</sup> and A. Zarrouk,<sup>2,\*</sup>**

<sup>1</sup>Laboratory of Advanced Materials and Process Engineering, Faculty of Sciences, Ibn Tofail University, P.O. Box. 133, Kenitra, 14000, Morocco

<sup>2</sup>Laboratory of Materials, Nanotechnology and Environment, Faculty of Sciences, Mohammed V University in Rabat, P.O. Box 1014, Agdal-Rabat, Morocco

<sup>3</sup>Higher Institute of Nursing Professions and Health Techniques of Agadir Annex Guelmim, Morocco

<sup>4</sup>Laboratory of Electronic Materials and Systems, Faculty of Science and Technology Department of Science and Materials, University of Mohamed El Bachir El Ibrahimi-El Anasser- Bordj Bou Arreridj, 34000, Algeria

<sup>5</sup>Ecole Normale Supérieure Assia Djebar of Constantine, Department of Physics and Chemistry, University Constantine 3, 250 00, Algeria

<sup>6</sup>Laboratory of Analytical Physicochemistry and Crystallochemistry of Organometallic and Biomolecular Materials, University Constantine 1, 250 00, Algeria

<sup>7</sup>Laboratory of Applied and Environmental Chemistry (LCAE), Mohammed First University, Oujda, Morocco

<sup>8</sup>Department of Chemistry, AN-Najah National University, P.O. Box 7, Nablus, Palestine

\*Corresponding Author, Tel.: +212537774261

E-Mail: [azarrouk@gmail.com](mailto:azarrouk@gmail.com)

*Received: 6 August 2023 / Received in revised form: 23 September 2023 /*

*Accepted: 24 September 2023 / Published online: 30 September 2023*

---

**Abstract-** The effects of 1.0 M hydrochloric acid (HCl) and 0.5 M sulphuric acid (H<sub>2</sub>SO<sub>4</sub>) were evaluated for a new pyran derivative known as (E)-4-hydroxy-3-(3-hydroxy-4-methoxyphenyl)acryloyl)-6-methyl-2H-pyran-2-one (HMAP) on corrosion of MS. To evaluate the efficacy of HMAP, various techniques including weight loss measurements, potentiodynamic polarization measurement (PP), electrochemical impedance spectroscopy

(EIS), and theoretical approaches [density functional theory (DFT) and Molecular Dynamic simulations (MDS)] were utilized. The maximum inhibitory efficiency was determined to be 89.3% in 1M HCl and 94.6% in 0.5M H<sub>2</sub>SO<sub>4</sub> at 298 K in the existence of 1 mM HMAP. Langmuir isotherm fitted well with the adsorption process. Plotting Nyquist and Bode graphs in EIS allowed to determine CPE parameters by fitting the resulting data. According to the polarization parameters, HMAP is a mixed-type inhibitor in both media, with a cathodic preponderance in the sulfuric medium. The results of the EIS investigation indicate that these compounds stop corrosion through an adsorption mechanism. Findings from experiments and theory were shown to be closely connected.

**Keywords-** New pyran derivative; HCl/H<sub>2</sub>SO<sub>4</sub>; Anticorrosion performance; Electrochemical impedance spectroscopy; Theoretical approaches

---

## 1. INTRODUCTION

Due to the characteristic abrasive quality of acid solutions, MS and iron corrosion research is both theoretical and practical. This kind of solution is often utilized in industry for a variety of tasks such as descaling, boiler cleaning with acid, acidification of oil wells and pickling [1–3]. For these purposes, acids like sulphuric and hydrochloric acids are typically utilized [4]. Numerous investigations have shown that a number of organic compounds are effective at preventing corrosion [5,6]. However, the bulk of them pose serious risks to the environment and human health. Natural materials are now employed as an alternative to chemical inhibitors for preventing corrosion because of the unfavorable effects [7]. Compounds with sulphur and nitrogen are better at stopping corrosion in acidic environments [8]. One of the most challenging aspects of utilizing carbon steel in applications is the material's very poor corrosion resistance in acid solutions. There are a variety of ways now in use to avoid corrosion of carbon steel. Organic inhibitors are one of the strategies that may be utilized to combat this problem [9,10]. The most potent inhibitors are heterocyclic compounds with bonds produced by phosphorus heteroatoms, as well as heteroatoms of nitrogen, sulphur, and oxygen [11–13]. In comparison to compounds containing either nitrogen or sulphur, compounds comprising both nitrogen and sulphur may provide superior inhibition [14–16]. According to the results, the majority of organic inhibitors have physically attached to metal surfaces by pushing water molecules away and establishing a thick barrier layer [17]. The accessibility to unbound electrons (isolated pair) and  $\pi$  in aromatic rings, alkynes alkenes in inhibitory molecules might imply chemisorption. Therefore, the electron density and polarizability of the functional group's donor atom were responsible for determining the force of the coordinated covalent bond [18]. It has been proved that heterocyclic chemicals including mercapto-triazole and 2-mercapto-1-methylimidazole [19] can effectively stop MS degradation in acidic solutions.

A novel pyran derivative used in this experiment represented HMAP. Subsequently, this evaluation made the analysis of the loss of weight, to the potentiodynamic polarization, to the spectroscopy of impedance electrochemical, DFT and to the simulations of dynamic molecular (MD), its inhibitory effect on MS corrosion in both harsh conditions was examined. The

purpose is to study any potential chemical corrosion inhibition mechanisms on MS in acidic solutions, as well as the link between inhibition performance and temperature.

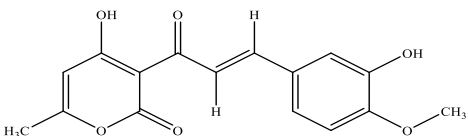
To better understand the adsorption mechanism of inhibitor molecules on the Fe corrosion surface at the atomic level, we calculated several thermodynamic and kinetic parameters to examine inhibitor adsorption on mild steel. We also examined the electronic structure, reaction activity and adsorption pattern of HMAP on the metal surface. The aforementioned research can provide fresh perspectives and new ideas for the design and building of new, highly effective inhibitors for the future, in addition to providing theoretical basis to the experimental results.

## 2. EXPERIMENTAL SECTION

### 2.1. Preparation of samples and materials

The process of diluting analytical reagent-grade H<sub>2</sub>SO<sub>4</sub> (98%) and HCl (37%) resulted in the formation of highly reactive solutions, namely a 0.5 M sulphuric acid solution and a 1.0 M chloridric acid solution, utilizing double-distilled water. In order to create a blank solution for comparison, the pyran derivatives are used in concentrations ranging from 10<sup>-3</sup> M to 10<sup>-6</sup> M with MS samples (C  $\approx$  0.0760%, Al  $\approx$  0.0230%, Mn  $\approx$  0.1920%, Si  $\approx$  0.022%, Cr  $\approx$  0.0500%, P  $\approx$  0.0120%, and Fe-balance) in rectangular dimensions 2.00 cm<sup>2</sup>  $\times$  0.20 cm used for weight loss and electrochemical tests [19]. Substrates underwent a preparation process involving cleaning with distilled water, degreasing with ethanol, and subsequent air-drying at room temperature. The substrates were abraded utilizing emery paper of various grades (180 to 2000 grain). Table 1 displays the inhibitor's molecular make-up for comparison.

**Table 1.** Abbreviation, IUPAC Name and the chemical structures of the pyran compound under study

Abbreviation	Chemical structure	IUPAC Name
HMAP		(E)-4-hydroxy-3-(3-(3-methoxyphenyl)acryloyl)-6-methyl-2H-pyran-2-one

### 2.2. Weight loss experiences

The first method to prevent metal corrosion in an acid solution is weight loss measurement. The samples must be immersed in a corrosive solution for six hours as part of this procedure.

The studies utilized 100 mL of solutions in solutions containing 0.5 M H<sub>2</sub>SO<sub>4</sub> or 1.0 M HCl at different inhibitor concentrations and in the absence of inhibitors. They were conducted in glass beakers.

In a thermostated water bath, the temperature of the electrolyte solution was maintained at 298 K. The steel specimens were carefully cleaned in accordance with ASTM standards before being reweighed at a mass of 10<sup>-4</sup> grams to assess corrosion rate (*CR*) [20]. Eq.1 and Eq.2 were utilized to estimate *CR* and inhibition efficiency  $\eta_{CR}$  % [21,22] :

$$CR = \frac{w_1 - w_2}{At} \quad \text{Eq. 1}$$

A represents the surface area (cm<sup>2</sup>) of the mild steel specimen, and the exposure duration is denoted by t (h). In addition, w<sub>1</sub> and w<sub>2</sub> correspond to the weight losses incurred before and after the immersion period, respectively.

$$\eta_{CR} \% = \left[ 1 - \frac{CR_{inh}}{CR} \right] \times 100 \quad \text{Eq. 2}$$

The corrosion rates *CR* and *CR*<sub>inh</sub> indicate the corrosion rate in the non-existence and existence of an inhibitor, respectively.

### 2.3. Electrochemical analysis

An electrochemical measurement (PDP or EIS) uses a potentiostat/galvanostat/PGZ 100 managed by the VoltaMaster 4 analysis software. The counter-electrode employed in the experiment was constructed using platinum foil, while the reference electrode utilized was a saturated calomel electrode (SCE). All potentials were given to the working electrodes, which were the MS samples. To achieve reproducible geometry, The electrodes are precisely positioned inside the cell. Additionally, immersing the working electrode in the test solution for 30 minutes allowed for the measurement of the open circuit potential to be made. Potentiodynamic polarization testing on MS specimens involved utilizing a scan rate of 1 mV/s to systematically vary the electrode potential from -0.9 to -0.1 V/SCE relative to the OCP. By extrapolation of the Tafel linear segments to the corrosion potential from both the anodic and cathodic curves allowed for the determination of the corrosion current density (*i*<sub>corr</sub>). The inhibitory efficiency was then calculated using the following equation [23]:

$$\eta_{pp} \% = \left[ 1 - \frac{i_{corr}}{i_{corr}^0} \right] \times 100 \quad \text{Eq. 3}$$

where *i*<sub>corr</sub> and *i*<sub>corr</sub><sup>0</sup> denote the values of corrosion current densities in the presence and absence of the organic molecule, respectively.

EIS measurements were conducted utilizing a transfer function analyzer, employing a low amplitude AC signal of 10 mV/ms, and employing a frequency range spanning from 10<sup>5</sup> Hz to

$10^{-1}$  Hz, with 10 points/decade. The Nyquist format was used to generate the graphs. The results were examined utilizing the ZView 2.80 program in relation to an analogous electrical circuit [24].

$$\eta_{imp} \% = \left[ 1 - \frac{R_p^0}{R_p} \right] \times 100 \quad \text{Eq. 4}$$

Where  $R_p$  and  $R_p^0$  represent the charge transfer resistances when HMAP is present and absent, respectively.

## 2.4. DFT and MD simulation details

Applying the DFT method within an aqueous environment, we tried to comprehend how the novel HMAP behaved on the MS surface [25]. This theoretical innovation also served to link the HMAP-determined experimental inhibitory efficacy to the chemical reactivity indices [26]. The examined molecule's structural structure has been altered by Gauss to take on its final form. Software package for the Gauss.09 model DFT/B3LYP/6-31G (d, p) [27].

The  $E_{HOMO}$ ,  $E_{LUMO}$ ,  $\Delta E_{gap}$ , total energy (TE), hardness ( $\eta$ ), electronegativity ( $\chi$ ), dipole moment ( $\mu$ ), dipole moment ( $\mu$ ) and ( $\Delta N_{110}$ ) are the electrons that are displaced from occupied orbitals of organic inhibitors to the unoccupied orbitals of metal surface. Where denotes the metallic bulk ( $\eta_{Fe110} = 0$  eV) and  $\Phi = \chi_{Fe110} = 4.82$  eV, the theoretical value of the work function for Fe(110) is given by (eq.8)[28].

$$\Delta E = E_{LUMO} - E_{HOMO} \quad \text{Eq. 5}$$

$$\chi = \frac{1}{2} (E_{LUMO} + E_{HOMO}) \quad \text{Eq. 6}$$

$$\eta = \frac{1}{2} (E_{HOMO} - E_{LUMO}) \quad \text{Eq. 7}$$

$$\Delta N_{110} = \frac{\chi_{Fe110} - \chi_{inh}}{2(\eta_{Fe110} + \eta_{inh})} = \frac{\Phi - \chi_{inh}}{2\eta_{inh}} \quad \text{Eq. 8}$$

Utilizing molecular dynamics (MD) modeling, we have studied the interaction between our HMAP/Fe<sub>110</sub> combination. Materials Studio2016's Forcite module was used to conduct these simulations [29,30]. These interactions for our studied system have been made in a simulation box that has the next dimensions  $32.27 \times 32.270 \times 30.13 \text{ \AA}^3$ , and each layer of the slab model's six layers represented a  $11 \times 11$  unit cell. This void is filled with 500H<sub>2</sub>O, 5H<sub>3</sub>O<sup>+</sup>, 5Cl<sup>-</sup> and D-Lim in HCl solution, and by 500 H<sub>2</sub>O, 10H<sub>3</sub>O<sup>+</sup>, and 5SO<sub>4</sub><sup>2-</sup> and D-Lim in H<sub>2</sub>SO<sub>4</sub> solution. Simulated system temperatures of 298 and 328 K were maintained using the Andersen thermostat, NVT set, with a simulation duration of 600 ps and a time step of 1.0 fs, while utilizing the COMPASS force field [31].

### 3. RESULTS AND DISCUSSION

#### 3.1. Gravimetric measurement

After 360 minutes of immersion in each harsh environment, the weight loss of MS corrosion was calculated both prior to and after the inclusion of different amounts of HMAP at 298K [32]. Furthermore, corrosion rate  $CR$  and inhibition efficiency  $\eta_{CR}$  % values are grouped in Table 2, respectively.

**Table 2.** Corrosion characteristics measured utilizing a gravimetric method on MS in in both aggressive environments with varying amounts existence or non-existence at 298 K

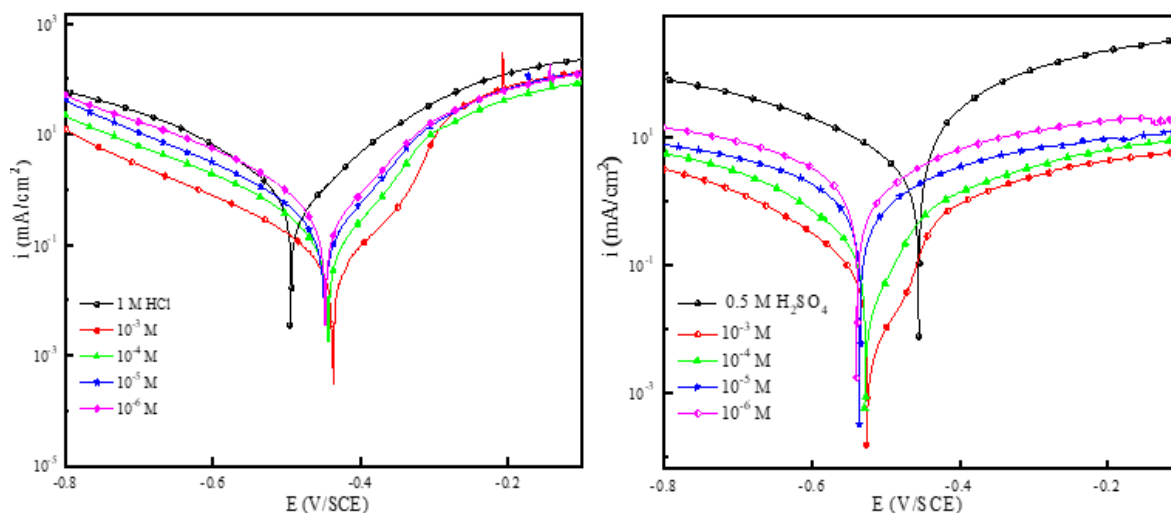
Medium	Concentration (M)	$CR$ (mg cm <sup>-2</sup> h <sup>-1</sup> )	$\eta_{CR}$ %
1 M HCl	0	5.6589	--
	10 <sup>-6</sup>	1.3355	76.4
	10 <sup>-5</sup>	1.0624	81.2
	10 <sup>-4</sup>	0.9983	82.4
	10 <sup>-3</sup>	0.6395	88.7
0.5 M H <sub>2</sub> SO <sub>4</sub>	0	10.5301	--
	10 <sup>-6</sup>	2.4595	56.5
	10 <sup>-5</sup>	1.8692	67.0
	10 <sup>-4</sup>	1.2812	77.4
	10 <sup>-3</sup>	0.7013	93.3

Table 2's observations revealed that as inhibitor concentration increased, corrosion rate decreased and inhibitory efficacy increased. Even at lower doses, the inhibitory efficiency was still detectable and reaching a maximum value of 88.7% in 1.0 M HCl and a value of 93.3% in 0.5 M H<sub>2</sub>SO<sub>4</sub>. This may be due to the greater adsorption of HMAP adsorption at the metal surface as their concentration increases in the two acid mediums could be the cause of this [33]. This shows that HMAP has a better inhibitory performance in the medium of sulfuric acid than in the medium of hydrochloric acid. The inhibitory performance  $\eta_{CR}$  % of this compound within the tested concentration rang is close to those reported for certain pyran derivatives in previous work [34–36].

#### 3.2. Electrochemical experiments

##### 3.2.1. Polarization studies

With the purpose of understanding the kinetics of the cathodic and anodic processes, polarization experiments were carried out in both aggressive environments not agitated, without and with varying concentrations of HMAP. The polarization curves obtained are displayed on the Figure 1.



**Figure 1.** MS-PP graphs at 298 K in both abrasive solutions, as well as in the absence and presence of various concentrations of HMAP

By extrapolating the cathodic and the anodic intercept of Tafel with  $E_{\text{corr}}$  and  $\eta_{\text{pp}}\%$ , the electrochemical parameters, as  $E_{\text{corr}}$  the both anodic & cathodic slopes of Tafel ( $\beta_a$ ) & ( $\beta_c$ ), and the corrosion current  $i_{\text{corr}}$ , as shown in Table 3, were obtained.

A comprehensive investigation of Figure 1 demonstrated that even in the non-existence of HMAP, MS displayed a maximum of anodic & cathodic currents. Furthermore, it was also observed that the compound slows down the anodic dissolution process in MS and retards the cathodic hydrogen evolution reaction [38], which may be connected to the adsorption of the HMAP molecule on the MS substrate and obstructs the active sites on the steel surface. This indicates that the hydrogen release process is not significantly impacted by the existence of this chemical. A charge transfer process is mostly utilized to reduce  $\text{H}^+$  ions on the surface of MS [39].

Table 3 shows that the  $E_{\text{corr}}$  values remain relatively constant in the existence of HMAP, this suggests that the pyran compound may function as a mixed-type inhibitor, with a predominance in the cathodic direction within the sulfuric medium. The cathode slope ( $\beta_c$ ) & anode slope ( $\beta_a$ ) readings don't really vary much when HMAP is present. This suggests that, without altering the mechanism of anodic or cathodic processes, HMAP adhesion on the surface of the MS lowers corrosion by reducing the number of active sites available for rusting. This table shows that the existence of HMAP causes a reduction of  $i_{\text{corr}}$  values and an increase in their corresponding  $\eta_{\text{pp}}$  up to 92.8% in 0.5 M  $\text{H}_2\text{SO}_4$  & 89.3% in 1.0 M HCl. These efficiencies are reached at a concentration of 1 mM HMAP. This finding shows that the inhibitor forms a barrier at the surface after adhering there, preventing mass and electron transit.

**Table 3.** The corrosion values determined by gravimetry of MS in aggressive solutions in the non-existence and in the existence of varied concentrations at 298 K

Medium	Conc. M	$-E_{\text{corr}}$ mV/SCE	$i_{\text{corr}}$ $\mu\text{A cm}^{-2}$	Tafel slopes ( $\text{mV dec}^{-1}$ )		$\eta_{\text{PP}}$ %
				$-\beta_{\text{c}}$	$\beta_{\text{a}}$	
1 M HCl	0	498	983	92	102	--
	$10^{-6}$	449	225	132	95	77.1
	$10^{-5}$	448	171	131	105	82.6
	$10^{-4}$	443	168	127	108	82.9
	$10^{-3}$	437	105	108	116	89.3
0.5 M H <sub>2</sub> SO <sub>4</sub>	0	451	1850	99	121	--
	$10^{-6}$	536	431	112	116	76.7
	$10^{-5}$	532	342	107	119	81.5
	$10^{-4}$	526	214	111	123	88.4
	$10^{-3}$	523	133	104	124	92.8

This table shows that the presence of HMAPs causes a reduction in  $i_{\text{corr}}$  values and a corresponding increase in  $\eta_{\text{pp}}$ , reaching up to 92.8% in a 0.5 M H<sub>2</sub>SO<sub>4</sub> solution and 89.3% in a 1.0 M HCl solution.

### 3.2.2. EIS measurements

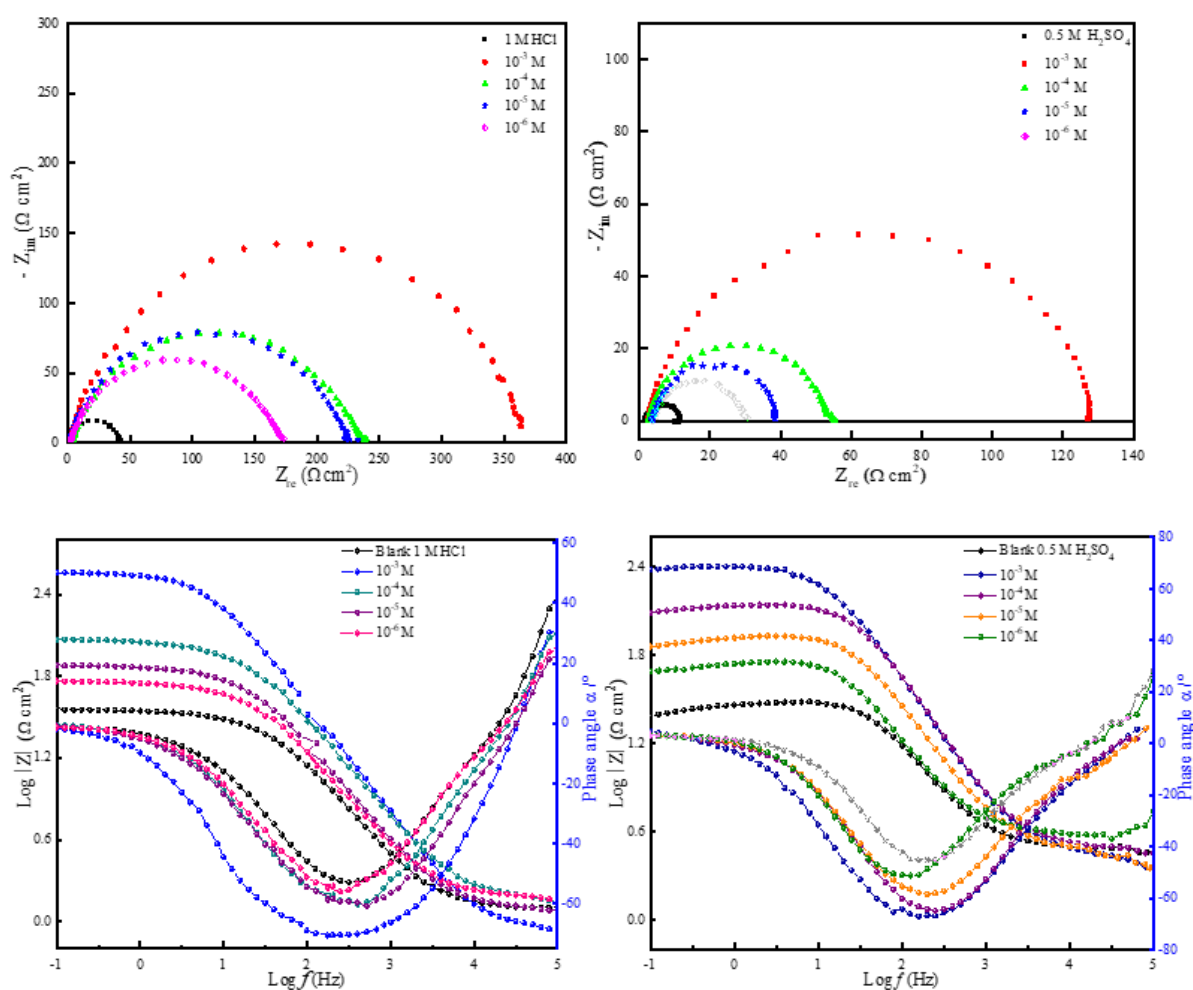
In this study, corrosion inhibition mechanisms were investigated utilizing electrochemical impedance measurements, which revealed details on the surface properties and kinetics of electrode actions. EIS were recorded at open circuit potential between 100 kHz & 100 mHz [37]. Figure 2 displays the Nyquist & Bode impedance curves for a 1.0 M HCl/MS system, both in the absence and in the presence of a range of HMAP concentrations. Similar diagrams for the 0.5 M H<sub>2</sub>SO<sub>4</sub>/MS system are offered.

Figure 2 shows the correlation between the equivalent circuit with a single constant-phase element at the metal/solution interface and the Bode plots. The increase in absolute impedance in the Bode curve at lower frequencies indicates better protection as the inhibitor concentration increases [39].

An analogous electrical circuit is used to represent the MS/solution interface based on the results of the Nyquist, Bode and phase diagrams. The results are shown in Figure 3 for the MS system with 1 M HCl/HMAP and for the MS system with 0.5 M H<sub>2</sub>SO<sub>4</sub>/HMAP. For the sulfuric medium (Figure 3b), composed of a solution resistor  $R_s$ , a constant phase element (CPE) in parallel with a parallel load transfer resistor  $R_{\text{ct}}$ , and an inductance resistor  $R_L$ , the latter in parallel with the inductance  $L$ , measured and simulated data reasonably align with each other.



It is common practice to use distributed circuit elements in the equivalent circuit when the frequency response is less than ideal [40].



**Figure 2.** The Nyquist & Bode plots for dissolution of MS in 1.0 M HCl and 0.5 M H<sub>2</sub>SO<sub>4</sub> with and without various doses of the compound HMAP at 298K.

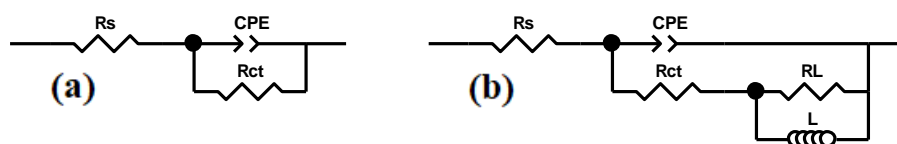


**Figure 3.** Equivalent circuit explored for simulating: (a) metal surface /1.0 M HCl/HMAP system (b) metal surface/0.5 M H<sub>2</sub>SO<sub>4</sub>/HMAP system

The ZView 2.80 software was used to analyze and interpret the Nyquist and Bode curves acquired from the MS electrodes immersed in unregulated acidic solutions treated with varying doses of HMAP. The corresponding electrical circuits, as seen below, were used for this

purpose. The introduction of the compound to the corrosive solution did not alter the corrosive environment process, according to the similarities between Nyquist plot shapes in the existence and non-existence of HMAP in the HCl environment. The existence of a unique semicircle demonstrates a unique charge transfer procedure throughout the dissolution process which is not impacted by the existence of inhibitory molecules. The Nyquist spectrum consists of a capacitive loop in HCl acid solutions and a single wave for the Bode plots. According to Nyquist diagrams, each impedance pattern in the sulfuric medium in with and without of an inhibitor consists of a large capacitive loop at high frequency (HF) and while low frequency (LF) has an inductive loop. In the non-existence of an inhibitor, two times constants for iron dissolution at  $E_{\text{corr}}$  have been described in some publications [41]. The HF capacitive loop might be caused by the double layer's capacitance running in parallel with the charge transfer resistance ( $R_{\text{ct}}$ ). The relaxation process that results from the adsorption of substances like  $H_{\text{ads}}^+$  &  $SO_4^{2-}$  on the metal surface may be the source of the inductive loop LF [42]. It might also be caused by the passivated surface's low-frequency re-dissolution [43]. The frequency dispersion effect, which is connected to surface roughness, inhibitor adsorption, or non-homogenization of the electrode surface, is a common name for the departure from a perfect circuit [38].

$$Z_{\text{CPE}} = Q^{-1} (i\omega)^{-n} \quad \text{Eq. 9}$$

In this context, the symbols  $n$ ,  $Q$ ,  $i$  &  $\omega$  represent the deviation index, the CPE constant, the imaginary number, and the angular frequency ( $2\pi f$ ), respectively. The  $C_{\text{dl}}$  values are also estimated by the formula [44]:

In this context, the symbols  $n$ ,  $Q$ ,  $i$  and  $\omega$  represent the deviation index, the CPE constant, the imaginary number, and the angular frequency ( $2\pi f$ ), respectively. The estimation of  $C_{\text{dl}}$  values is also conducted using the formula:

$$C_{\text{dl}} = \left[ Q \times (R_{\text{ct}})^{1-n} \right]^{1/n} \quad \text{Eq. 10}$$

Table 4 provides the most necessary information acquired from the equivalent circuits. Note that whereas  $R_{\text{ct}}$  rises with the concentration of the inhibitor,  $C_{\text{dl}}$  declines until the optimal concentration is achieved ( $10^{-3}$  M) indicates that more inhibitor molecules are adsorbed.

Table 4 clearly shows that as inhibitor concentration increases, the values of  $R_{\text{ct}}$  increased significantly, while the values of  $Q$  decreased. The striking rise in  $R_{\text{ct}}$  values denotes the gradual creation of a protective adsorption film as well as an increase in the quantity of inhibitor molecules that are adsorbed on the electrode surface with increasing inhibitor concentration. The rise in electrical double layer thickness and the decrease in the local dielectric constant are responsible for the decrease in  $Q$  values, which implies that the inhibitor molecule acts by adsorbing at the metal/solution interface [45]. As expected, the  $\eta$  value progressively increased with the increasing concentration of inhibitor. This result is in good concurrence with the findings derived from the weight loss and polarization measurements.

**Table 4.** EIS parameters for the mild steel after immersion in 1 M HCl & 0.5 M H<sub>2</sub>SO<sub>4</sub> solutions with different concentrations of HMAP at 298 K

Medium	Conc (M)	R <sub>s</sub> ( $\Omega$ cm <sup>2</sup> )	Q ( $\Omega^{-1}$ s <sup>n</sup> cm <sup>2</sup> )	n	C <sub>dl</sub> ( $\mu$ F cm <sup>2</sup> )	R <sub>ct</sub> ( $\Omega$ cm <sup>2</sup> )	R <sub>L</sub> ( $\Omega$ cm <sup>2</sup> )	L (H)	$\eta_{imp}$ %	$\theta$
1 M HCl	0	1.1	419.0	0.773	121.0	40.0	-	-	-	-
	10 <sup>-6</sup>	1.4	237.3	0.765	94.4	169.7	-	-	76.5	0.765
	10 <sup>-5</sup>	1.0	187.3	0.795	79.0	223.7	-	-	82.2	0.822
	10 <sup>-4</sup>	0.9	176.5	0.768	64.7	231.9	-	-	82.8	0.828
	10 <sup>-3</sup>	0.8	103.3	0.886	58.6	361.5	-	-	88.9	0.889
0.5 M H <sub>2</sub> SO <sub>4</sub>	0	1.6	430.0	0.830	180.0	11.7	2.17	0.480	-	-
	10 <sup>-6</sup>	3.9	192.3	0.878	115.4	47.0	8.40	1.352	55.5	0.555
	10 <sup>-5</sup>	3.6	128.7	0.910	61.2	72.0	15.0	3.231	66.6	0.666
	10 <sup>-4</sup>	2.3	97.3	0.863	57.2	121.6	18.5	6.726	77.5	0.775
	10 <sup>-3</sup>	2.5	82.2	0.873	45.3	217.2	40.1	42.01	90.7	0.907

### 3.2.3. Effect of temperature and activation parameters

It is crucial for a corrosion inhibitor's use that it be stable in a hostile environment at specific operating temperatures. Temperature is a factor that might alter the activity of inhibitors and substrates in an aggressive environment at the same time. As a result, a rise in temperature would encourage the desorption of the inhibitor and result in the quick breakdown of the organic compounds or complexes created, decreasing the steel's corrosion resistance [46]. We performed electrochemical characterisation at various temperatures (298 - 328 K) to assess the impact of this variable on the inhibitor efficacy on steel. The polarization curves obtained with a concentration of 10<sup>-3</sup> M at different temperatures in both acid media with and without HMAP are shown in Figure 4 and also the Table 5 displays the data extracted from these polarization curves.

The findings presented in Table 5 demonstrate that, over the whole temperature range investigated, the value of the corrosion current density rises as temperature rises; thus, the inhibitory effectiveness  $\eta_{pp}(\%)$  marginally declines as temperature rises. The beneficial effect on corrosion phenomenon can be utilized to explain this. Similar to this, the quick desorption of HMAP molecules from the steel surface is responsible for the decrease in inhibitory effectiveness [47].

To calculate the activation energy ( $E_a$ ) associated with corrosion, it is necessary to compute the  $i_{corr}$  values at various temperatures. This analysis may provide valuable insights on the adsorption process. The following equation delineates the correlation between temperature and corrosion rate [48]:

$$i_{corr} = Ae^{\frac{-E_a}{RT}} \quad \text{Eq. 10}$$

$$\ln i_{corr} = \ln A - \frac{E_a}{RT} \quad \text{Eq. 11}$$

where  $E_a$  denotes the activation energy, the absolute temperature ( $T$ ), the pre-exponential Arrhenius factor ( $A$ ) and the universal gas constant ( $R$ ).

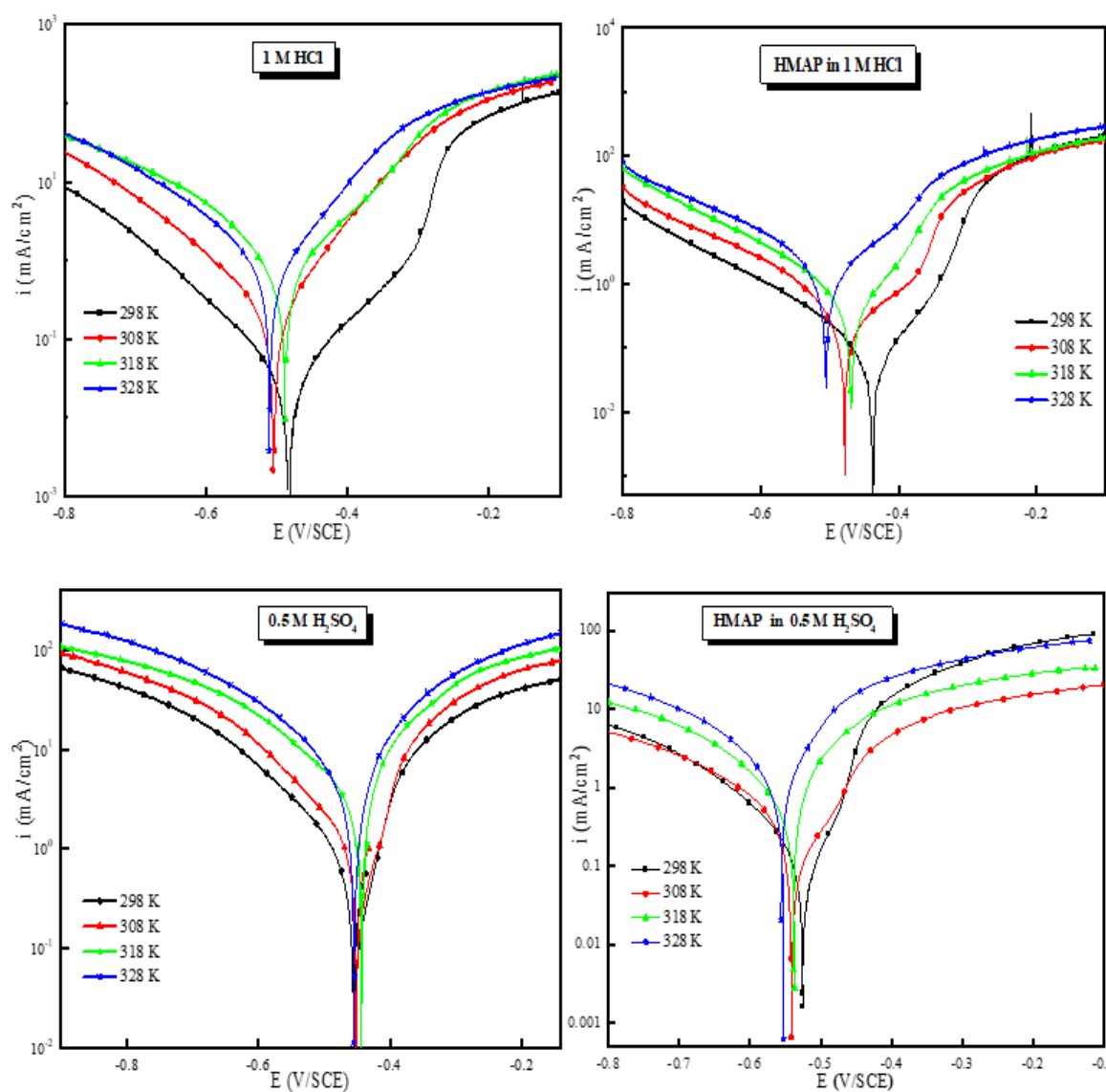


**Figure 4.** Curves of polarization generated for MS in both aggressive environments in both environments the (absence and presence) of HMAP at various temperatures

Equation 13 can be changed to produce a straight line, which enables the Arrhenius relation to be utilized to compute the apparent activation energy.

**Table 5.** Tafel fitting data for MS at various temperatures for 1 mM HMAP in 1.0 M HCl & 0.5 M H<sub>2</sub>SO<sub>4</sub>

Medium	T (K)	-E <sub>corr</sub> (mV/SCE)	i <sub>corr</sub> (μA cm <sup>-2</sup> )	Tafel slopes (mV dec <sup>-1</sup> )		η <sub>pp</sub> (%)
				-β <sub>c</sub>	β <sub>a</sub>	
1.0 M HCl	298	498	983	92	104	—
	308	491	1200	184	112	—
	318	475	1450	171	124	—
	328	465	2200	161	118	—
1.0 M HCl + HMAP	298	437	105	108	116	89.3
	308	478	152	100	104	87.3
	318	468	214	144	90	85.2
	328	505	392	152	113	82.2
0.5 M H <sub>2</sub> SO <sub>4</sub>	298	451	1850	99	121	—
	308	453	2250	92	114	—
	318	449	2480	96	102	—
	328	442	3340	102	97	—
0.5 M H <sub>2</sub> SO <sub>4</sub> + HMAP	298	523	133	104	124	92.8
	308	540	228	109	125	89.8
	318	535	328	111	122	86.7
	328	552	539	115	120	83.8

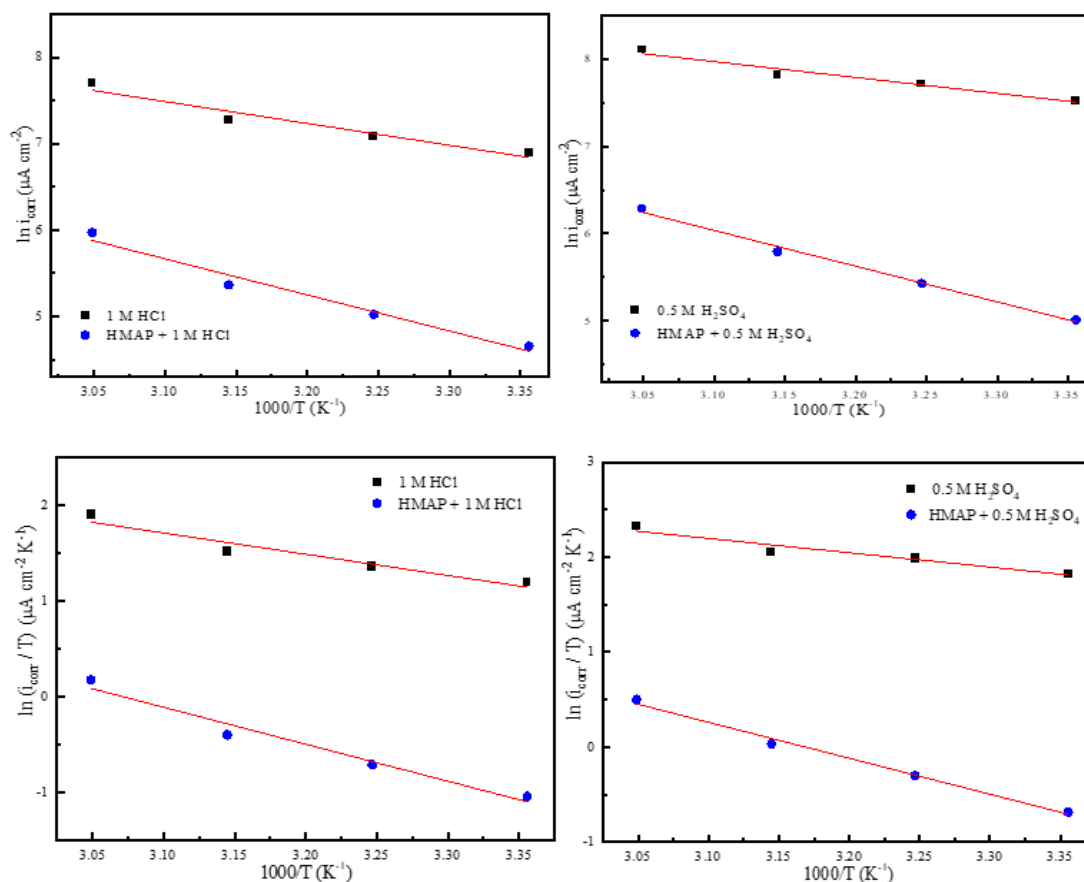
**Figure 5.** Arrhenius lines for MS in both aggressive environments in the existence and non-existence 1 mM of HMAP

Figure 5 shows the relation between the corrosion current density ( $i_{\text{corr}}$ ) and the inverse of the temperature ( $T$ ). The enthalpy and entropy values are calculated based on the Arrhenius line, which is based on the change of  $\ln\left(\frac{i_{\text{corr}}}{T}\right)$  versus  $\left(\frac{1000}{T}\right)$ , which is the straight line between the blank and the inhibitor being studied [49].

$$\ln\left(\frac{i_{\text{corr}}}{T}\right) = \left[ \ln\left(\frac{R}{hN_a}\right) + \left(\frac{\Delta S_a}{R}\right) \right] - \frac{\Delta H_a}{RT} \quad \text{Eq. 13}$$

Where  $N_a$  Avogadro number, enthalpy of activation  $\Delta H_a$ ,  $h$  is Planck constant & the entropy of activation  $\Delta S_a$ .

Table 6 lists the activation energy for 0.5 M  $\text{H}_2\text{SO}_4$  & 1.0 M  $\text{HCl}$  both, without the inhibitor and its presence. With the addition of derivative pyran in both 0.5 M  $\text{H}_2\text{SO}_4$  & 1.0 M  $\text{HCl}$ , the apparent activation energies ( $E_a$ ) for mild steel in the acidic medium both, without and with the addition of  $10^{-3}$  M HMAP show an increase. This phenomenon can be elucidated by the increase in the energy barrier when the organic molecule is present and the electrostatic adsorption mechanism of the inhibitor onto the MS surface [50]. While the growing value of  $\Delta H_a$  up on the addition of HMAP indicates a decrease in the dissolving of the metal, the endothermic process of corrosion was confirmed by the positive value of  $\Delta H_a$ . Additionally, The decrease in entropy during the transition of the activated reaction to a complex of iron molecules in solution can be used to explain the high and negative  $\Delta S_a$  values observed in the inhibited solution [51].

**Table 6.** Activation parameters for MS dissolution in both aggressive environments without and with of  $10^{-3}$  M HMAP

Parameters	$E_a$ (kJ mol <sup>-1</sup> )		$\Delta H_a$ (kJ mol <sup>-1</sup> )		$\Delta S_a$ (J mol <sup>-1</sup> K <sup>-1</sup> )	
	1 M HCl	0.5 M $\text{H}_2\text{SO}_4$	1 M HCl	0.5 M $\text{H}_2\text{SO}_4$	1 M HCl	0.5 M $\text{H}_2\text{SO}_4$
Blank	21	15	18.5	12.5	-126	-140.5
$10^{-3}$ M of HMAP	34.75	34	32.2	31.5	-98.76	-97.79

### 3.3. Adsorption isotherm

To find out the manner in which the inhibitor binds to the metal surface, the application of adsorption isotherms is essential. The Langmuir, Temkin, Freundlich, Frumkin, and El Awady isotherms are widely used for this purpose [49].

These isotherms obey a fundamental expression which is defined by the following equation [52]:

$$f(\theta, x)e^{-2a\theta} = K_{ads}C_{inh} \quad \text{Eq. 12}$$

In this context, the term ' $f(\theta, x)$ ' represents the correlation factor, which is determined by the physical model and basic hypotheses used to derive the isotherm. The parameter known as ' $a$ ' plays a key role in assessing the interactions of molecules with the adsorption surface and in evaluating the level of surface heterogeneity.

Where  $K_{ads}$  denotes the adsorption coefficient,  $f$  is the energy inhomogeneity factor (' $f > 0$ ' means lateral attraction between adsorbed organic molecules and ' $f < 0$ ' indicates repulsion between adsorbed molecules), ' $a$ ' is the number of water molecules that an inhibitory organic molecule replaces (also known as the size ratio parameter),  $C_{inh}$  is the concentration of the inhibitor in the solution,  $n$  is the adsorption intensity, and  $\theta$  is the extent to which the mild steel surface is covered by an inhibitor molecule. To find the best isotherm to simulate inhibitor adsorption on MS, the adsorption isotherm models were examined. The EIS measurement is utilized to calculate the recovery rate [53]. Figure 6 depicts the graphical depiction of the tested Langmuir isotherm's linear equations, and Table 7 lists the parameter values that were taken from this figure.

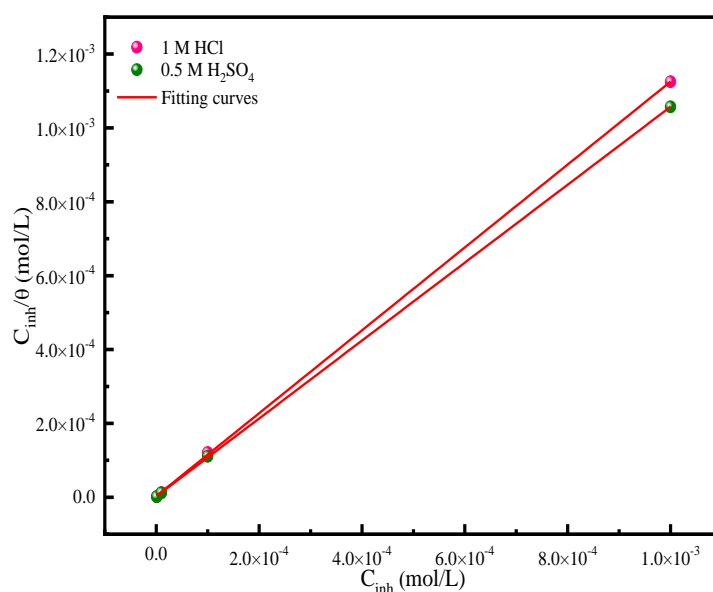


**Figure 6.** Adsorption isotherms for MS at 298K in both aggressive environments for the studied concentrations of HMAP.

However, the equation 15 was utilized to determine the standard free energy  $\Delta G_{ads}^0$  value.

$$\Delta G_{ads}^0 = -RT \ln(55.55 \times K_{ads}) \quad \text{Eq. 13}$$

T is the temperature (K), 55.55 mol/L indicates the molar concentration of water in solution and R is the ideal gas constant (J/K mol).

**Table 7.** Thermodynamic values for the adsorption of HMAP on the MS surface in both aggressive environments at 298 K

Isotherm	Parameters	1 M HCl	0.5 M H <sub>2</sub> SO <sub>4</sub>
Langmuir	R <sup>2</sup>	0.99996	0.99998
	Slope	1.12234	1.05521
	K (L/mol)	3.282×10 <sup>5</sup>	4.636×10 <sup>5</sup>
	$\Delta G_{ads}^0$ (KJ/mol)	-41.42	-42.28

The Langmuir model appears to be the best acceptable among the examined isotherms for characterizing the adsorption of pyran compound, and the experimental data are superbly adjusted with a slope close to 1 and associated parameters (Table 6). According to this model, the HMAP inhibitor is suggested to create a protective monolayer on the steel's surface through adsorption, thereby inhibiting corrosion [54].

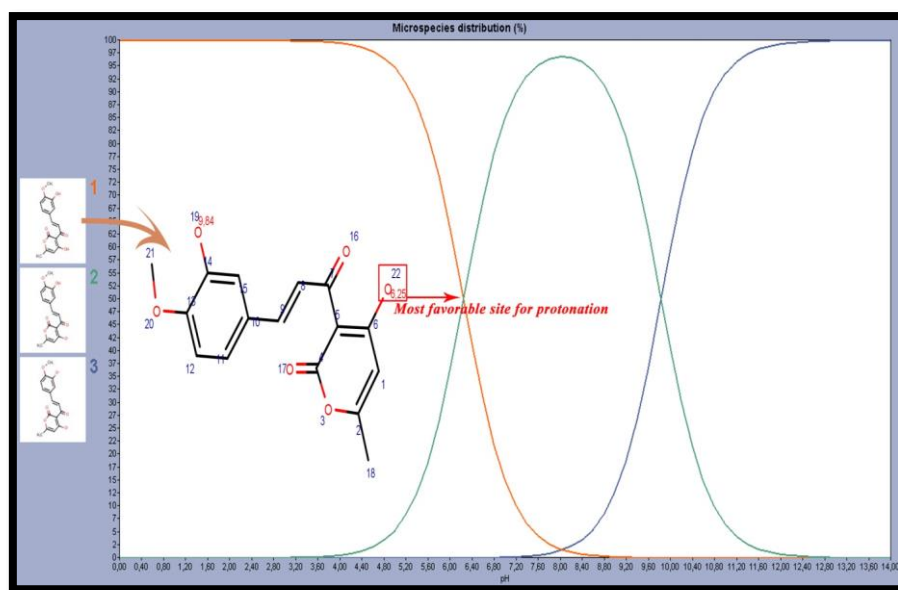
Typically, when the absolute value of  $\Delta G_{ads}^0$  approaches or is more negative than -40 kJ mol<sup>-1</sup>, it indicates that the adsorption of inhibitor molecules demonstrates chemisorption characteristics [54,55]. Conversely, when the absolute value of  $\Delta G_{ads}^0$  is -20 kJ mol<sup>-1</sup> or less negative, the adsorption is categorized as physisorption due to electrostatic interactions [54,55]. The  $\Delta G_{ads}^0$  measured for HMAP in both aggressive environments at 298 K in the Langmuir model yields values closer to -40 kJ/mol, suggesting that this inhibitor chemically binds to the steel surface, forming bonds that hinder the penetration of corrosive substances [52].

### 3.3. DFT study

#### 3.3.1. Global reactivity

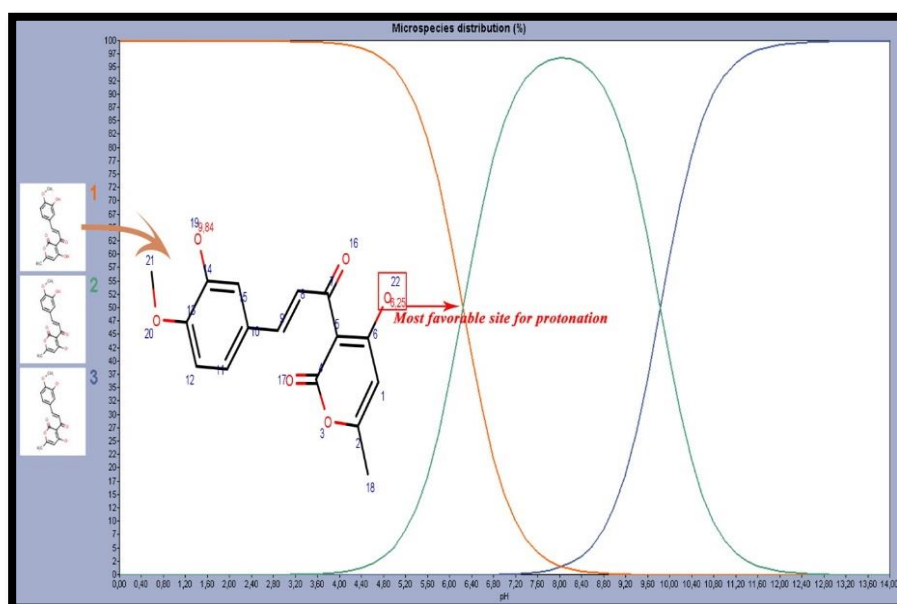
Quantum chemical computations have been utilized to analyze a molecule's electrical characteristics and determine its local and overall chemical reactivity [56]. The molecule studied (HMAP) in this work appears to belong to pyran derivatives. These derivatives are very active against corrosion due to the planar geometry of the base molecule (pyran) [57]. Quantum chemical descriptors were utilized to determine the HMAP's overall reactivity, while methods such as Fukui indices and molecular electrostatic potential were employed to examine the reactivity at the local level. Most organic molecules are protonated in acidic mediums, if this requires the determination of the favourable site(s) available for protonation, then the HMAP is protonated in the oxygen atom O(22) as shown in Figure 7, O(22) is considered a more relevant site for protonation, this site was determined utilizing MarvinView software. The protonated atom is able to interact with the metal surface through electrostatic bonds.





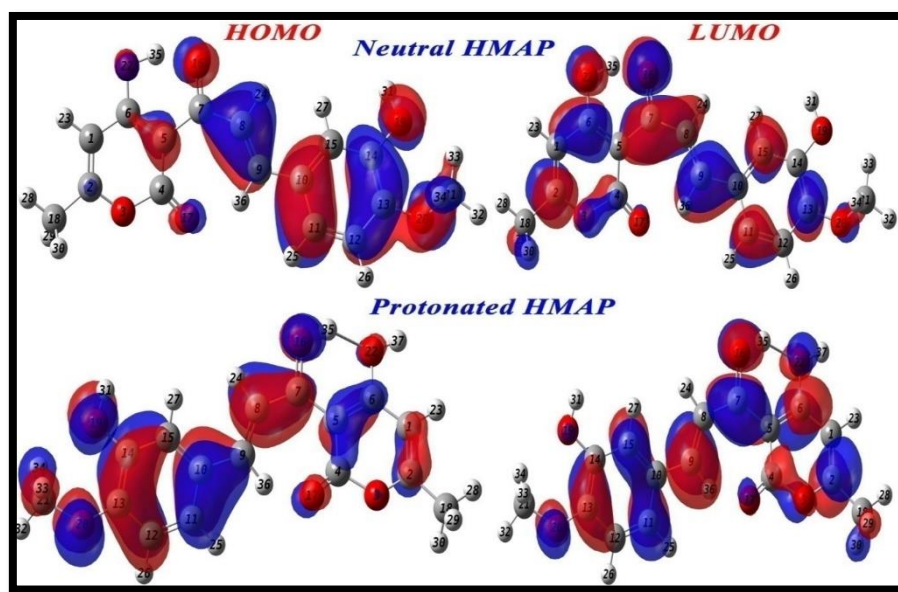
**Figure 7.** Active sites available for protonation

Figure 8 displays the neutral and protonated variants of the HMAP's optimized structures. It is obvious that protonation influences the special geometry of the neutral molecule. It's evident that protonation has a significant impact on the molecule's geometry. This is evidenced by the shorter bond lengths observed in the protonated form, suggesting that it is more stable than the neutral form. The lower total energy value of HMAP (+1) further supports this assertion. Consequently, the charged form exhibits higher chemical reactivity compared to the non-protonated form.



**Figure 8.** Optimized HMAP configurations in the protonated and neutral states

According to the findings from the literature review, frontier molecular orbitals (FMOs), specifically HOMO and LUMO, are frequently used in research focusing on the structural chemical reactivity of a molecule. These orbitals can be used to identify specific reactive regions distributed over the molecular surface, these sites are responsible for adsorption on the metal surface [58]. The electron density distribution of the FMOs of two studied forms of the HMAP molecule is given in Figure 9. It is well noticeable that all the structure of the neutral form of HMAP except the donor group by inductive effect  $\text{CH}_3$  is occupied by the electron densities of HOMO & LUMO, indicating that this surface is rich in active donor and acceptor centers. This result shows that the neutral form is possibly adsorbed parallel to the metal surface, enhancing the protection of the steel surface examined. As far as the protonated form is concerned, the structure of the protonated molecule is totally occupied by the electron density of the FMOs. Which shows that protonation increases the distributed electron density distribution, consequently the reactivity increases compared to the neutral form, i.e., the protonated molecule is somewhat more favorable to adsorption on the substratum.



**Figure 9.** FMOs of the HMAP molecule in two forms, protonated and neutral.

Table 8 compiles the significant values of the quantum chemical descriptors. The inclusion of these characteristics is of utmost importance when assessing the overall chemical reactivity of the HMAP molecule in two studied forms [59]. The electron donor ability is examined by the electron donor altitudes of the descriptors  $E_{\text{HOMO}}$  &  $\Delta N_{110}$ , wherein the high values of these descriptors indicate that the molecule in question in two forms is capable of giving the electrons to the vacant iron orbitals in order to establish the most rigid bonds, favouring the most efficient adsorption on the metal surface [60]. As per Table 8, the  $\Delta N_{110}$  value of the protonated form is superior to that of the neutral form, which informs that the charged molecule has more electron

donating power despite the site protonation which is very active such as O (22). This implies that protonation is efficiently conducted to increase the electron donating capacity, i.e. more reactivity with the metal surface. While the molecule's ability to accept electrons is assessed by  $E_{\text{LUMO}}$ , meaning that the higher the minimum value of this descriptor, the higher the altitude for receiving electrons, as shown in Table 8, the protonated form has a greater ability to receive electrons from the occupied orbitals of the iron atom than the neutral compound. [61].

In addition, a low value of the gap energy ( $\Delta E$ ) indicates a high reactivity of the molecule, which reinforces the adsorption of the protonated form of HMAP on the metal surface, indicating that the adsorption mechanism is very stable [62].

Another crucial term that expresses a molecule's polarity and links it to adsorption ability is the dipole moment ( $\mu$ ) [63]. Therefore, a high value of can enhance the adsorption between the two forms of the HMAP molecule and the steel surface. As a result, the substantial dipole moment value may induce an electron transfer from the protonated molecule to the metal surface. In addition, when the HMAP molecule attaches to the metal surface, the direction of the dipole moment vector is changed based on the adsorption configuration.

**Table 8.** Quantum chemical descriptors of the HMAP molecule in two forms, protonated and neutral

Molecular forms	$E_{\text{HOMO}}$ (eV)	$E_{\text{LUMO}}$ (eV)	$\Delta E$ (eV)	$\Delta N_{110}$	$\mu$ (D)	TE (a.u)
HMAP	-6.068	-2.421	3.647	2.485	2.031	-1069.737
HMAP (+1)	-8.952	-6.360	2.582	3.511	6.900	-1070.102

### 3.3.2. MEP and Fukui indices site actives

Local reactivity (reactive sites) was evaluated using Fukui indices and molecular electrostatic potential [64]. The MEP is generally represented by regions such as positive regions with low total density (blue color), negative regions with high total density (red color) and intermediate regions with medium density (other colors)[65]. The topographic distribution of the total density of MEP is given in Figure 10. The condensed Fukui functions are calculated utilizing the GGA function with the DNP (3.5) basis set in Materials Studio<sup>2016</sup> equipment and based on Mulliken population analysis. The density of the compacted Fukui functions and the Fukui indices of the atoms in the protonated and neutral forms of the HMAP molecule are presented in Figure 10 and Table 9, respectively. By analysis of the calculated Fukui indices ( $f_k^+$ ,  $f_k^-$ ) of the HMAP molecule in the neutral and the protonated forms, for the first form, It is evident that the maximal density of the C (8), C (9), C (11), C (13), O (19), and O (20) atoms, which are regarded as electron donor sites, is  $f_k^-$ . While ( $f_k^+$  is at its highest for the atoms C (2), C (6), C (7), C (9), O (16), and O (22) suggesting that these locations likely

take electrons. Regarding the second form (protonated), new local sites with the same condensed functionalities, such as C (2), C (8), O (16), and O (17), are appearing. This reveals that these locations serve as both electron donation and acceptance sites. Additionally, the majority of the sites are dispersed throughout the protonated molecule's whole skeleton.

The MEP is also shown in Figure 10, As this figure shows, the red regions correspond to active sites where electrons are donated, and these sites are responsible for electrophilic attacks, while the blue regions contain electron acceptor sites, facilitating nucleophilic attacks.

After protonation, the molecular surface carries the positive charge, reflecting the ability to accept electrons. All of these findings collectively indicate that both forms possess active local electron donor and acceptor sites, which play a significant role in their strong adsorption onto the metal surface.

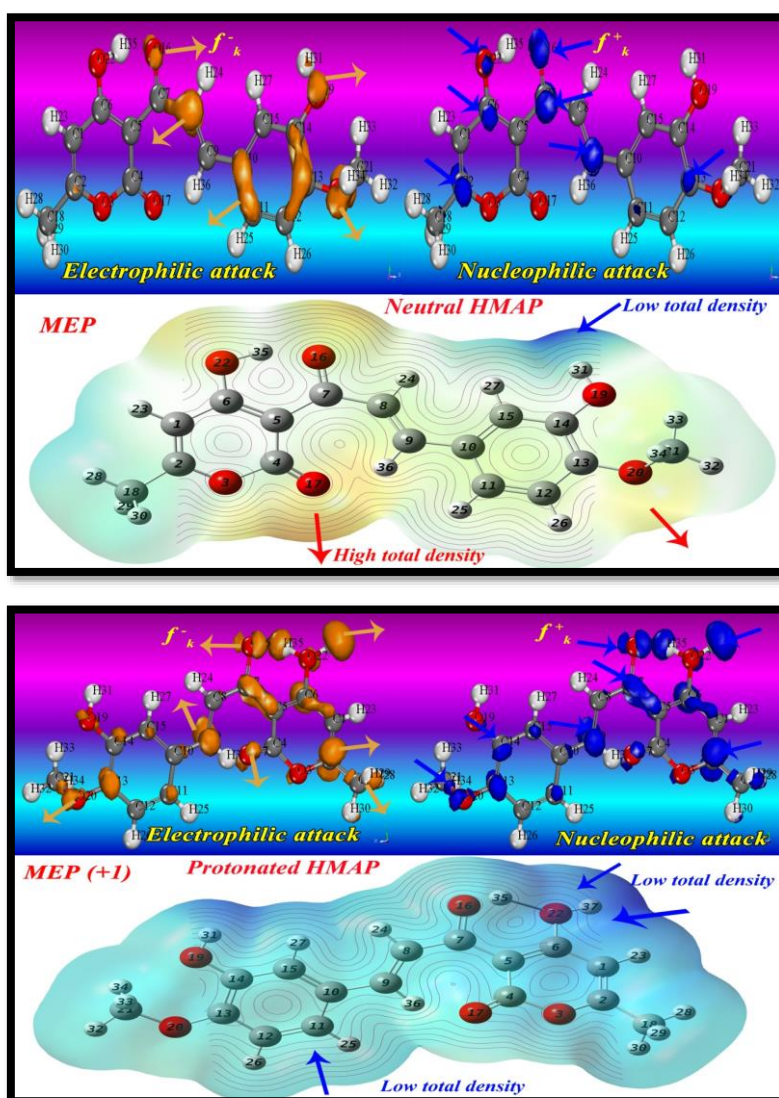


**Figure 10.** Condensed Fukui functions and MEP distributions of neutral (HMAP) and protonated (HMAP (+1)) forms

**Table 9.** Fukui indexes for  $f_k^+$  &  $f_k^-$  of neutral (HMAP) and protonated (HMAP (+1)) forms calculated at GGA/DNP

Atoms	indexes	C (1)	C (2)	O (3)	C (4)	C (5)	C (6)	C (7)	C (8)	C (9)	C (10)	C (11)
$f_k^+$	HMAP	0.028	0.053	0.028	0.017	0.015	0.047	0.073	0.027	0.073	0.009	0.031
	HMAP (+1)	0.029	0.059	0.031	0.015	0.026	0.039	0.037	0.017	0.048	0.005	0.026
$f_k^-$	HMAP	0.014	0.019	0.014	0.009	0.009	0.016	0.018	0.078	0.022	0.056	0.060
	HMAP (+1)	0.029	0.059	0.031	0.015	0.027	0.040	0.034	0.018	0.047	0.005	0.026
Atoms	indexes	C (12)	C (13)	C (14)	C (15)	O (16)	O (17)	C (18)	O (19)	O (20)	C (21)	O (22)
$f_k^+$	HMAP	0.026	0.043	0.021	0.026	0.081	0.033	0.018	0.023	0.027	0.012	0.055
	HMAP (+1)	0.025	0.037	0.019	0.023	0.053	0.044	0.018	0.021	0.026	0.010	0.033
$f_k^-$	HMAP	0.042	0.062	0.047	0.024	0.040	0.011	0.008	0.058	0.072	0.023	0.030
	HMAP (+1)	0.024	0.036	0.019	0.022	0.051	0.045	0.018	0.021	0.027	0.010	0.033

### 3.3.3. MD simulations

Molecular dynamics simulations were used to study how the HMAP molecule interacts with the metal structure, in order to improve our understanding of the adsorption mechanism [66]. This simulation was run utilizing hydrochloric and sulfuric acids as the simulated acidic media, under the influence of temperature in order to know, in the first case, the influence of the aggressivity of the acid milieu on energy potentials (see Table 10), and in the second case, the effect of temperature on the bonds that are formed between an adsorbate molecule's active sites and iron atoms (see Figures 11 and 12). Figures 11 & 12 illustrate the optimal adsorption configurations of the HMAP molecule on the Fe (110) surface, representing the ideal equilibrium in the acidic media being examined. The conclusion of our quantum chemical calculation that the under-researched molecule has multiple active sites dispersed over the entire molecular surface is supported by the fact that all configurations represented in both media and under the influence of two temperatures are localized parallel and above on the metal surface. Therefore, the surface that the tested molecule covers is essential for effectively protecting the metal surface. All of these findings support the assertion that the HMAP molecule operates consistently across the two investigated media. This explains why the value of the HMAP molecule's corrosion inhibitory activity is crucial.



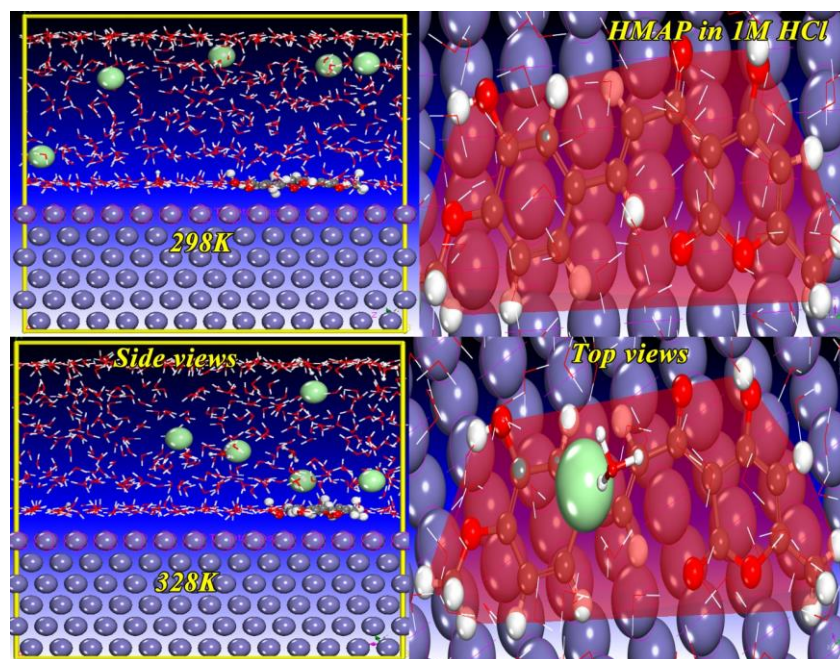


**Figure 11.** The HMAP's optimal equilibrium adsorption arrangements on the surface of Fe (110) in 1.0 M HCl solution

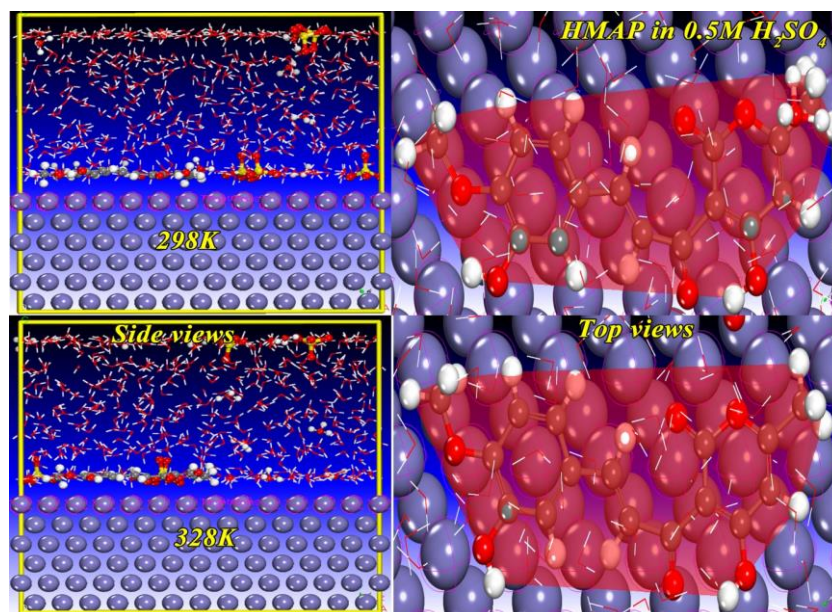


**Figure 12.** Optimized equilibrium adsorption configurations of the HMAP onto the Fe (110) surface in 0.5 M H<sub>2</sub>SO<sub>4</sub> solution

The values of the interaction ( $E_{\text{interaction}}$ ) and binding ( $E_{\text{binding}}$ ) energies under the influence of media aggressiveness and temperature, are grouped together in Table 10.

The absorption process occurs spontaneously, with parallel orientation being preferred, as evidenced by the negative values of  $E_{\text{interaction}}$  between the HMAP and the surface of Fe (110)

[67]. In addition, the value of the  $E_{\text{interaction}}$  is more inferior in HCl than in  $\text{H}_2\text{SO}_4$ . This indicates that the sulphuric medium is more aggressive than the hydrochloric medium, i.e. more corrosive. Similarly, the increase in temperature influences the molecule/surface interactions, resulting in an increase in the  $E_{\text{interaction}}$  value. In both corrosive mediums, this behavior also manifested itself. The degree of the HMAP's adsorption on the metal surface is often explained by the binding energy [68]. The combined data in Table 10 demonstrate that the  $E_{\text{binding}}$  values in the hydrochloric acid media are positive and raised, which demonstrates an HMAP adsorption force on the iron surface and denotes a reduction in the inhibitory ability of the under investigated molecule.

**Table 10.** MD simulation results of system-HMAP in HCl &  $\text{H}_2\text{SO}_4$  at 298 K & 328 K, MD simulation results of System-HMAP in HCl &  $\text{H}_2\text{SO}_4$  at 298 K & 328 K

MD simulation results	HMAP in 1 M HCl		HMAP in 0.5 M $\text{H}_2\text{SO}_4$	
	$E_{\text{interaction}}$	$E_{\text{binding}}$	$E_{\text{interaction}}$	$E_{\text{binding}}$
System-HMAP+298K	-821.196	821.196	-212.197	-212.197
System-HMAP+328K	-802.533	802.533	-191.641	-191.641

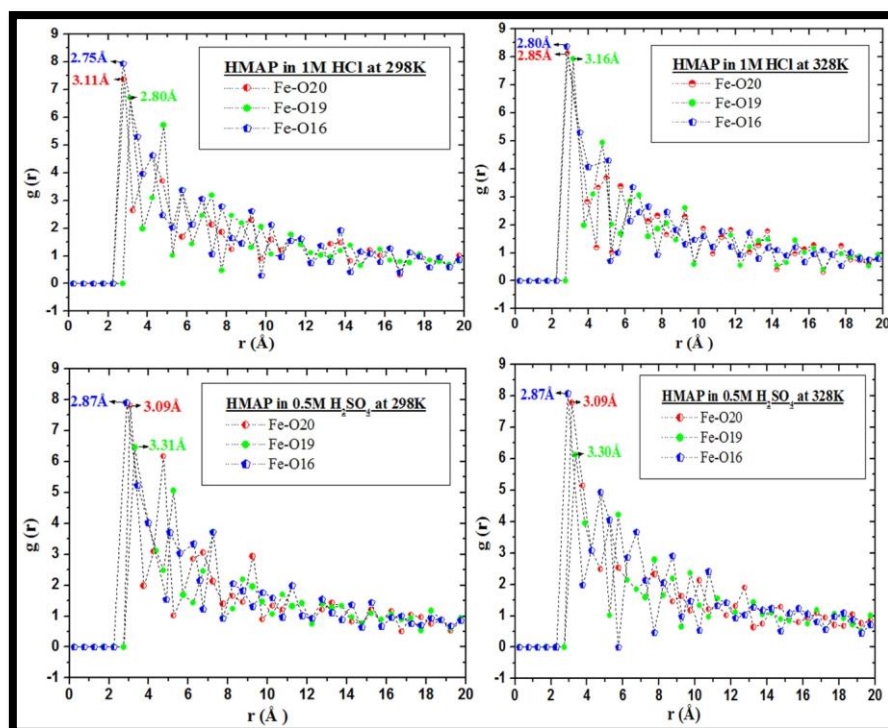


**Figure 13.** RDF of HMAP /Fe (110) in HCl &  $\text{H}_2\text{SO}_4$  at 298 & 328 K

The link lengths between HMAP and the iron atoms in the initial layer of Fe (1 1 0) were calculated [69] using the radial distribution function (RDF) method. Based on a review of existing literature, the nature of the interaction between substances Q and N is considered as chemisorption if the initial peak resulting from this interaction is detectable in the  $g_{QN}(r)$  graph against the  $r$  distance and falls within the range of 1 to 3.5 Å, and physisorption if the peaks appear at positions higher than 3.5 Å [70,71]. The results of the RDF are presented in Figure 13. In the RDF produced for the interactions of  $g(r)_{\text{Fe (110)-HMAP}}$  in HCl and H<sub>2</sub>SO<sub>4</sub> at 298 and 328 K with the iron surface atoms, the first peak inferior to 3.5 Å is clearly seen in this image. This HMAP chemisorption encourages the growth of a barrier-like layer that protects the steel under test from the corrosion process on the surface of Fe (1 1 0).

#### 4. CONCLUSION

The effects of pyran-2-one derivatives on mild steel corrosion in the presence of 1.0 M HCl & 0.5 M H<sub>2</sub>SO<sub>4</sub> in acidic environments were investigated, it was found that these substances are excellent MS corrosion inhibitors in these environments, with maximum inhibition efficiencies exceeding 89.3% in 1.0 M HCl & 94.6% in 0.5 M H<sub>2</sub>SO<sub>4</sub>. The inhibitor's presence (at a concentration of  $10^{-3}$  M of HMAP), which increased  $R_{ct}$  and decreased  $C_{dl}$  values in the EIS findings, demonstrates that HMAP prevents MS corrosion by erecting a barrier at the MS-Electrolyte interface. The chemical HMAP possesses a characteristic that prohibits both cathodic and anodic reactions with a cathodic majority in the sulfuric medium, according to polarization curves. The isothermal Langmuir model foresees HMAP adsorption on metallic surfaces. The result of  $\Delta G_{ads}^0$  [ $-41.33 \text{ kJ mol}^{-1}$ ] shows that chemisorption is mostly responsible for HMAP adsorption on smooth surfaces. The inhibition of the soluble pyran derivative in water was evaluated utilizing a mix of experimental and theoretical techniques. The results of DFT and MD are supported by the results of the experiments. We were able to show a substantial correlation between the estimated descriptors for the studied chemical compounds and their inhibition rates as a result of our quantitative analysis on HMAP. all the theoretical calculations reveal that the compound with a small energy gap shows a high inhibitory efficacy.

#### Declarations of interest

The authors declare no conflict of interest in this reported work.

#### REFERENCES

- [1] F.E. Abeng, M.E. Ikpi, O.A. Ushie, V.C. Anadebe, B.E. Nyong, M.E. Obeten, N.A. Okafor, V.I. Chukwuike, and P.Y. Nkom, Chem. Data Collect. (2021) 100722.
- [2] I.B. Obot, and N.O. Obi-Egbedi, Corros. Sci. 52 (2010) 198.
- [3] L. Türker, S. Gümüş, and T. Atalar, J. Energ. Mater. 28 (2010) 139.



- [4] J. Aljourani, M.A. Golozar, and K. Raeissi, *Mater. Chem. Phys.* 121 (2010) 320.
- [5] T.W. Quadri, L.O. Olasunkanmi, O.E. Fayemi, E.D. Akpan, C. Verma, E.S.M. Sherif, K.F. Khaled, and E.E. Ebenso, *Coord. Chem. Rev.* 446 (2021) 214101.
- [6] X. Li, S. Deng, and H. Fu, *Corros. Sci.* 53 (2011) 302.
- [7] M.A. Quraishi, A. Singh, V.K. Singh, D.K. Yadav, and A.K. Singh, *Mater. Chem. Phys.* 122 (2010) 114.
- [8] A. Zarrouk, B. Hammouti, A. Dafali, and H. Zarrok, *Der Pharma Chem.* 3 (2011) 266.
- [9] A. Tazouti, M. Galai, R. Tourir, M.E. Touhami, A. Zarrouk, Y. Ramli, M. Saraçoğlu, S. Kaya, and F. Kandemirli, C. Kaya, *J. Mol. Liq.* 221 (2016) 815.
- [10] M. Rbaa, F. Benhiba, I.B. Obot, H. Oudda, I. Warad, B. Lakhrissi, and A. Zarrouk, *J. Mol. Liq.* 276 (2019) 120.
- [11] A. Zarrouk, B. Hammouti, A. Dafali, and H. Zarrok, *Der Pharma Chem.* 3 (2011) 266.
- [12] D.S. Chauhan, P. Singh, and M.A. Quraishi, *J. Mol. Liq.* 320 (2020) 114387.
- [13] R. Nabah, F. Benhiba, Y. Ramli, M. Ouakki, M. Cherkaoui, H. Oudda, R. Tourir, I. Warad, and A. Zarrouk, *Anal. Bioanal. Electrochem.* 10 (2018) 1375.
- [14] G. Avci, *Colloids Surfaces A Physicochem. Eng. Asp.* 317 (2008) 730.
- [15] N. Dkhireche, M. Galai, Y. El Kacimi, M. Rbaa, M. Ouakki, B. Lakhrissi, and M. Ebn Touhami, *Anal. Bioanal. Electrochem.* 10 (2018) 111.
- [16] 16. M. El Faydy, F. Benhiba, B. Lakhrissi, M.E. Touhami, I. Warad, F. Bentiss, and A. Zarrouk, *J. Mol. Liq.* 295 (2019) 111629.
- [17] S.A. Ali, H.A. Al-Muallem, M.T. Saeed, and S.U. Rahman, *Corros. Sci.* 50 (2008) 664.
- [18] K. Sadik, S. Byadi, M.E. Hachim, N. El Hamdani, Č. Podlipnik, and A. Aboulmouhajir, *J. Mol. Struct.* 1240 (2021) 130571.
- [19] H. Zarrok, A. Zarrouk, R. Salghi, H. Oudda, B. Hammouti, M. Ebn Touhami, M. Bouachrine, and O.H. Pucci, *Port. Electrochim. Acta* 30 (2012) 405.
- [20] A. Zarrouk, T. Chelfi, A. Dafali, B. Hammouti, S.S. Al-Deyab, I. Warad, N. Benchat, and M. Zertoubi, *Int. J. Electrochem. Sci.* 5 (2010) 696.
- [21] K. Cherrak, M.E. Belghiti, A. Berrissoul, M. El Massaoudi, M. El Faydy, M. Taleb, S. Radi, A. Zarrouk, and A. Dafali, *Surf. Interfaces* 20 (2020) 100578.
- [22] R. Salim, A. Nahlé, F. El-Hajjaji, E. Ech-chihbi, F. Benhiba, F. El Kalai, N. Benchat, H. Oudda, A. Guenbour, M. Taleb, I. Warad, and A. Zarrouk, *Surf. Eng. Appl. Electrochem.* 57 (2021) 233.
- [23] J.N. Asegbeloyin, P.M. Ejikeme, L.O. Olasunkanmi, A.S. Adekunle, and E.E. Ebenso, *Materials (Basel)*. 8 (2015) 2918.
- [24] A. Majjane, D. Rair, A. Chahine, M. Et-tabirou, M. Ebn Touhami, and R. Tourir, *Corros. Sci.* 60 (2012) 98.
- [25] H.M. Abd El-Lateef, M.A. Abo-Riya, and A.H. Tantawy, *Corros. Sci.* 108 (2016) 94.
- [26] M. Rbaa, F. Benhiba, R. Hssisou, Y. Lakhrissi, B. Lakhrissi, M.E. Touhami, I. Warad,

- and A. Zarrouk, *J. Mol. Liq.* 322 (2021) 114549.
- [27] Y. Kharbach, F.Z. Qachchachi, A. Haoudi, M. Tourabi, A. Zarrouk, C. Jama, L.O. Olasunkanmi, E.E. Ebenso, and F. Bentiss, *J. Mol. Liq.* 246 (2017) 302.
- [28] O. Fergachi, F. Benhiba, M. Rbaa, R. Tourir, M. Ouakki, M. Galai, B. Lakhrissi, H. Oudda, and M.E. Touhami, *Mater. Res.* 21 (2018) 1.
- [29] Z. Rouifi, M. Rbaa, A.S. Abousalem, F. Benhiba, T. Laabaissi, H. Oudda, B. Lakhrissi, A. Guenbour, I. Warad, and A. Zarrouk, *Surf. Interfaces* 18 (2020) 100442.
- [30] M.S. 2017, *Materials Studio*, Revision 8.0, Accelrys Inc., San Diego, USA, 2017.
- [31] H.C. Andersen, *J. Chem. Phys.* 72 (1980) 2384.
- [32] P. Singh, D.S. Chauhan, S.S. Chauhan, G. Singh, and M.A. Quraishi, *J. Mol. Liq.* 286 (2019) 110903.
- [33] A. Zarrouk, H. Zarrok, R. Salghi, R. Tourir, B. Hammouti, N. Benchat, L. L. Afrine, H. Hannache, M. El Hezzat, and M. Bouachrine, *J. Chem. Pharm. Res.* 5 (2013) 1482.
- [34] A. El Hattak, S. Izzaoui, Z. Rouifi, F. Benhiba, S. Tabti, A. Djedouani, N. Komih, H. Abou El Makarim, R. Touzani, H. Oudda, I. Warad, and A. Zarrouk, *Chem. Data Collect.* 32 (2021) 100655.
- [35] M.A. Migahed, S.M. Elsaeed, A.M. Al-Sabagh, E.A. Khamis, and E.G. Zaki, *Res. J. Pharm., Biol. Chem. Sci.* 7 (2016) 1669.
- [36] M. Khattabi, F. Benhiba, S. Tabti, A. Djedouani, A. El Assyry, R. Touzani, I. Warad, H. Oudda, and A. Zarrouk, *J. Mol. Struct.* 1196 (2019) 231.
- [37] G.S. Masaret, B.A. Al Jahdaly, *J. Mol. Liq.* (2021) 116534.
- [38] S. El Arrouji, K. Karrouchi, A. Berisha, K. Ismaily Alaoui, I. Warad, Z. Rais, S. Radi, M. Taleb, M. Ansar, and A. Zarrouk, *Colloids and Surfaces A* 604 (2020) 125325.
- [39] J. Porcayo-Calderon, E.M. Rivera-Muñoz, C. Peza-Ledesma, M. Casales-Diaz, L.M. Martínez de la Escalera, J. Canto, and L. Martinez-Gomez, *J. Electrochem. Sci. Technol.* 8(2) (2017) 133.
- [40] K.F. Khaled, K. Babić-Samardžija, and N. Hackerman, *Corros. Sci.* 48 (2006) 3014.
- [41] S.A. Umoren, Y. Li, and F.H. Wang, *Corros. Sci.* 52 (2010) 2422.
- [42] P.C. Okafor, and Y. Zheng, *Corros. Sci.* 51 (2009) 850.
- [43] E.M. Sherif, and S.M. Park, *Electrochim. Acta* 51 (2006) 1313.
- [44] Popova, M Christov, and A Vasilev, *Corros. Sci.* 53 (2011) 1770.
- [45] B. Wang, M. Du, and J. Zhang, C.J. Gao, *Corros. Sci.* 53 (2011) 353.
- [46] F. Benhiba, H. Serrar, R. Hsissou, A. Guenbour, A. Bellaouchou, M. Tabyaoui, S. Boukhris, H. Oudda, I. Warad, and A. Zarrouk, *Chem. Phys. Lett.* 743 (2020) 137181.
- [47] A. Saady, E. Ech-chihbi, F. El-Hajjaji, F. Benhiba, A. Zarrouk, Y.K. Rodi, M. Taleb, A. El Biache, and Z. Rais, *J. Appl. Electrochem.* 51 (2021) 245.
- [48] L. Koursaoui, Y. Kerroum, M. Tabyaoui, A. Guenbour, A. Bellaouchou, B. Satrani, M. Ghanmi, I. Warad, A. Chaouch, and A. Zarrouk, *Biointerface Res. Appl. Chem.* 11

- (2021) 10119.
- [49] S.A. Umoren, M.J. Banera, T. Alonso-Garcia, C.A. Gervasi, and M. V. Mirifico, *Cellulose* 20 (2013) 2529.
- [50] Y. ELouadi, F. Abridach, A. Bouyanzer, R. Touzani, O. Riant, B. ElMahi, A. El Assyry, S. Radi, A. Zarrouk, and B. Hammouti, *Der Pharma Chem.* 7 (2015) 265.
- [51] H. M. Abd El-Lateef, K. A. Soliman, and A. H. Tantawy, *J. Mol. Liq.* 232 (2017) 478.
- [52] K. Boumhara, H. Harhar, M. Tabyaoui, A. Bellaouchou, A. Guenbour, and A. Zarrouk, *J. Bio- Tribo-Corrosion.* 5 (2019) article number 8.
- [53] A. Khadiri, A. Ousslim, K. Bekkouche, A. Aouniti, I. Warad, A. Elidrissi, B. Hammouti, F. Bentiss, M. Bouachrine, and A. Zarrouk, *J. Bio- Tribo-Corrosion.* 4 (2018) article number 64.
- [54] Z. Rouifi, F. Benhiba, M. El Faydy, T. Laabaissi, H. Oudda, B. Lakhrissi, A. Guenbour, I. Warad, and A. Zarrouk, *Ionics* 27 (2021) 2267.
- [55] Y. Yan, X. Wang, Y. Zhang, P. Wang, X. Cao, and J. Zhang, *Corros. Sci.* 73 (2013) 123.
- [56] F. Benhiba, Y. Elaoufir, M. Belayachi, H. Zarrok, A. El Assyry, A. Zarrouk, B. Hammouti, E.E. Ebenso, A. Guenbour, Al Deyab, Al Deyab, and H. Oudda, *Der Pharm. Lett.* 6 (2014) 306.
- [57] K.E. Anwer, A.A. Farag, E.A. Mohamed, E.M. Azmy, and G.H. Sayed, *J. Ind. Eng. Chem.* 97 (2021) 523.
- [58] H.M. Abd El-Lateef, and A.O. Alnajjar, *J. Mol. Liq.* 303 (2020) 112641.
- [59] Z. Rouifi, M. Rbaa, F. Benhiba, T. Laabaissi, H. Oudda, B. Lakhrissi, A. Guenbour, I. Warad, and A. Zarrouk, *J. Mol. Liq.* 307 (2020) 112923.
- [60] M.M. Khalaf, A.H. Tantawy, K.A. Soliman, and H.M. Abd El-Lateef, *J. Mol. Struct.* 1203 (2020) 127442.
- [61] L.O. Olasunkanmi, I.B. Obot, M.M. Kabanda, and E.E. Ebenso, *J. Phys. Chem. C.* 119 (2015) 16004.
- [62] A. Berrissoul, E. Loukili, N. Mechbal, F. Benhiba, A. Guenbour, B. Dikici, A. Zarrouk, and A. Dafali, *J. Colloid Interface Sci.* 580 (2020) 740.
- [63] D.K. Verma, S. Kaya, E. Ech-chihbi, F. El-Hajjaji, M.M. Phukan, and H.M. Alnashiri, *J. Mol. Liq.* 329 (2021) 115531.
- [64] H. Rahmani, K.I. Alaoui, M. EL Azzouzi, F. Benhiba, A. El Hallaoui, Z. Rais, M. Taleb, A. Saady, B. Labriti, A. Aouniti, and A. Zarrouk, *Chem. Data Collect.* 24 (2019) 100302.
- [65] A.E.L. Yaktini, A. Lachiri, M.E.L. Faydy, F. Benhiba, H. Zarrok, M.E.L. Azzouzi, M. Zertoubi, M. Azzi, B. Lakhrissi, and A. Zarrouk, *Orient. J. Chem.* 34 (2018) 3016.
- [66] M. Murmu, S.K. Saha, N.C. Murmu, and P. Banerjee, *Corros. Sci.* 146 (2019) 134.
- [67] T. Laabaissi, F. Benhiba, Z. Rouifi, M. Rbaa, H. Oudda, H. Zarrok, B. Lakhrissi, A.

- Guenbour, I. Warad, and A. Zarrouk, *Prot. Met. Phys. Chem. Surfaces* 55 (2019) 986.
- [68] M. Abdallah, A. Al Bahir, H.M. Altass, A. Fawzy, N. El Guesmi, A.S. Al-Gorair, F. Benhiba, I. Warad, and A. Zarrouk, *J. Mol. Liq.* 330 (2021) 115702.
- [69] F. El-Hajjaji, E. Ech-chihbi, N. Rezki, F. Benhiba, M. Taleb, D.S. Chauhan, and M.A. Quraishi, *J. Mol. Liq.* 314 (2020) 113737.
- [70] J. Saranya, F. Benhiba, N. Anusuya, R. Subbiah, A. Zarrouk, and S. Chitra, *Colloids Surfaces A Physicochem. Eng. Asp.* 603 (2020) 125231.
- [71] V. Mehmeti, and F.I. Podvorica, *Materials* 11 (2018) 893.